

Failure mode transition in Opalinus Clay: a hydro-mechanical and microstructural perspective

Lisa Winhausen¹, Kavan Khaledi¹, Mohammadreza Jalali¹, Janos L. Urai², Florian Amann^{1,3}

¹ Department of Engineering Geology and Hydrogeology, RWTH Aachen University, Lochnerstraße 4-20, 52064 Aachen, Germany.

² Institute of Tectonics and Geodynamics, RWTH Aachen University, Lochnerstraße 4-20, 52064 Aachen, Germany.

³ Fraunhofer IEG, Fraunhofer Research Institution for Energy Infrastructures and Geothermal Systems IEG, Kockerellstraße 17, 52062 Aachen, Germany

Correspondence to: Lisa Winhausen (winhausen@lih.rwth-aachen.de)

Abstract. The way rocks deform under changing stress conditions can be described by different deformation modes, which is fundamental for understanding their rheology. For Opalinus Clay, which is considered as a potential host rock for nuclear waste, we investigate the failure mode as a function of applied effective stress in laboratory experiments. Therefore, we performed consolidated-undrained triaxial tests at different effective consolidation stresses from 2.5 to 16 MPa, in which samples were loaded parallel to bedding, and analysed the deformation structures using ion-beam polishing and electron microscopy. With increasing effective confining stress, the results show a transition from brittle-dominated to more ductile-dominated deformations, localising in distinct shear bands. Both effective stress paths and microstructural analysis indicate a tendency towards less dilation in the shear zones for higher effective stresses. Triaxial test results suggest a non-linear failure envelope. The non-linearity of the failure envelope is associated with decreasing dilation with increasing effective stress accompanied by changes in microstructural deformation processes, which explain the decreasing friction angle. For the first time, we can verify that the observed non-linear failure envelope is due to the gradual transition from brittle- to more ductile-dominated deformation on the microscale controlling the bulk hydro-mechanical behaviour of Opalinus Clay.

Many shales and other clay-rich rocks are considered ~~as~~ natural barriers in geo-engineering applications such as the disposal of nuclear waste (e.g. Sellin and Leupin, 2013). Therefore, a proper description of the material's properties and behaviour is required for developing constitutive models to predict its physical behaviour upon effective stress changes. Past studies analysed the hydro-mechanical and failure behaviour of clay-rich rocks considered as host rocks for nuclear waste disposal (e.g., Amann et al., 2012; Bésuelle et al., 2014; Wild and Amann, 2018a; Braun et al., 2021). Here, a crucial aspect is the failure mode transition controlled by brittle- to ductile-dominated mechanisms and their implications on the microstructural development of the deforming geomaterial.

For clay-rich rocks under controlled laboratory conditions, the style of deformation has been inferred from the bulk (hydro-) mechanical response such as stress-strain curves and effective stress paths as well as macroscopic inspections of failed samples (Tchalenko, 1970; Niandou et al. 1997; Nygard et al., 2006; Amann et al., 2012; Wild and Amann, 2018a; Wild and Amann, 2018b). However, comprehensive models including structural changes and processes on the microscale level have not been developed so far.

The transition between failure modes and style of deformation has been analysed for many rock types such as sandstone, limestone, marble, and igneous rocks (e.g. [Heard, 1960](#); [Handin et al., 1963](#); Gramberg, 1965; Wong et al., 1997). Controlling factors for the style of deformation are effective stress, temperature, strain rate, fluid content and type of fluid (Evans et al., 1990). [In rock mechanics](#), ~~T~~three post-failure deformation modes are usually distinguished, which are the brittle, the semi-brittle or brittle-ductile, and the ductile mode. In triaxial compression, stress-strain curves show a distinct post-failure stress drop for the brittle mode (as opposed to the ductile mode) due to the strain-softening behaviour. [Griggs and Handin \(1960\) related the failure modes based on varying capabilities to withstand permanent strain before failure. Heard \(1960\) differentiated failure modes based on maximum \(axial\) strain at failure. According to his definition, the specimen is classified as brittle, transitional or ductile, if failure occurred at less than 3 %, between 3 % and 5 %, or above 5 % strain, respectively.](#) From a structural perspective, the spatial distribution of inelastic strain changes from localised shear fractures in the brittle field to semi-brittle flow and eventually to ~~fully plastic~~[uniform](#) flow without localised deformation and zero dilatancy in the ductile field (Evans et al., 1990). On a microscale, brittle deformation is typically associated with cataclasis including micro-cracking and grain comminution, as opposed to distributed micro-cracking, twinning, flattening and bending of grains, which are the prominent mechanisms in ductile deformation (Yongnian et al., 1989; Menéndez et al., 1996; Wong et al., 1997). Over the decades, many models have been developed to predict the transition between these failure modes (e.g., Gramberg, 1965; Mogi, 1966, [Byerlee, 1968](#); Goetze, 1971). For clay-rich geomaterials, the type of deformation is furthermore influenced by the consolidation state (Ingram and Urai, 1999; Nygard et al., 2006). Accordingly, over-consolidated clays tend to brittle failure and normal-consolidated clays tend to fail in ductile manner. [A critical discussion on the use of the terms “brittle” and “ductile” has been raised by Rutter \(1986\), who pointed to the often misused nomenclature for the above described failure modes when using the criteria of the rock’s capacity to withstand non-localized strain or the mechanistic approach implying the deformation](#)

mechanism. He underlined his argumentation with the scale-dependent types of deformation. Instead, he proposed to use the terms “brittle/cataclastic to plastic” failure modes. However, in the geomechanical context of this study, the term “plastic or plasticity” refers to non-elastic, permanent strain, which would – strictly speaking – also include fractures. For this reason, we stick to the previously stated terminology, but we will explain the use of such in the description and discussion of our results.

Major findings on shear-induced structures in clays have been made by Skempton (1966), Morgenstern and Tchalenko (1967) and Tchalenko (1968), who showed that shearing results in complex fabrics including kinks bands, the formation of multiple slip surfaces and shear lenses. Clays, natural and remoulded, have been further investigated on the micrometre-scale in SEM studies focusing on fabric changes upon uniaxial and triaxial loading. Different deformation processes can be identified, e.g., porosity reduction due to pore collapse of inter- and intra-aggregate pores of clay aggregates (Delage and Tessier, 2020), progressive reorientation of clay particles (Djéran-Maigre et al., 1998; Hattab and Fleureau, 2011), and the breakage of inter-aggregate bonds between clay aggregates (Hattab et al. 2013). Compared to clays, however, clay-rich rocks and especially shales are often characterised by a considerable maturity due to their burial history and diagenetic processes, and may show a different macro- and microscale deformation behaviour. In addition, the microstructural deformation and underlying processes of clay-rich materials are complex because of i) the polymineralic nature with contrasting mineral stiffnesses leading to elastic mismatches between different grains (Kranz 1983), and ii) the anisotropy due to preferred pore and mineral orientation (Attewell and Sandford, 1974).

Recent high-resolution microstructural studies on clay-rich rocks deformed under triaxial compression provide insight into the deformation structures and associated mechanisms, which include micro-cracking, grain bending and rotation, as well as particulate flow localised within distinct shear zones (Desbois et al., 2017; Oelker, 2020; Schuck et al., 2020; Winhausen et al., 2021). Winhausen et al. (2021) found from microstructural analysis of an Opalinus Clay sample deformed under triaxial compression that brittle and ductile failure mechanisms at grain-scale may coexist, i.e. micro-cracking and bending of phyllosilicates. This coexistence and the effective stress-dependent deformation microstructures found in other shales (Ibanez and Kronenberg, 1993; Petley, 1999) suggest a transitional failure behaviour on the microscale likely due to increasing effective confining stresses. The influence of effective stresses on failure mode and micro-deformation processes was, however, so far not systematically analysed. This study attempts to relate the abovementioned processes on the microscale to the hydro-mechanical deformation behaviour of Opalinus Clay under various effective stresses.

2 Materials and Methods

2.1 Material description and preparation

Opalinus Clay (OPA) from the Mont Terri Underground Research Laboratory in Switzerland is a soft clay shale formation, whose shaly facies is characterised by a dark-gray, clay-dominated matrix with silt- to sand-sized components like quartz,

90 mica and feldspar grains, and calcite bioclasts such as fossil shells (Houben et al., 2014; Lauper et al., 2021). The mineralogy is mainly composed of 50–70 % clay minerals, 10–20 % quartz, 7–25% carbonate and a minor amount of accessory minerals such as titanite, pyrite, and feldspars (Thury and Bossart, 1999; Klinkenberg et al., 2009). A large portion of the porosity is present in the clay matrix, which follows a power-law distribution with pore areas in the range of a few square-nanometres and smaller (Houben et al., 2014). The pronounced macro- and microscopic bedding, governed by the preferred orientation of
95 grains and pores, causes a transversal-anisotropic, hydro-mechanical behaviour (Sarout et al., 2014; Wild and Amann, 2018a).

2.2 Experimental Procedure

The experimental assemblage consisted of a pressure vessel, two pressure generators for confining oil and pore water pressure, and an electro-mechanical axial load generator (i.e. servo motor). The system was operated using a 14 kHz digital controller. Figure 1 shows the experimental setup consisting of the pressure cell containing the sample and the in-vessel sensor
100 assemblage.

The samples with dimensions of 60 mm length and 30 mm diameter were jacketed by a fluorine rubber (FKM) sleeve sealed from the confining oil fluid. Displacements were measured by three axial LVDTs (linear variable differential transformer) and a diametral extensometer. To avoid corrections for the deformation of the jacket, the radial sensor is in contact with the sample by steel plugs, which are embedded in the rubber sleeve. Two pressure transducers were installed at the top and bottom of the
105 sample to measure the fluid pressure. For a uniform pore fluid distribution along the sample surface, sintered stainless-steel plates were placed above and below the sample (Fig. 1). An artificial brine was prepared after Mäder (2011), which was used to re-saturate the samples. The axial load was measured by an internal load cell of 100 kN capacity situated below the sample. This way, frictional forces between piston and sealing are excluded from the measurement. The experiments were conducted under a constant ambient temperature of 30° C in a climate chamber.

110 Macroscopically intact P-samples, i.e., the maximum principal stress is applied parallel to the samples' long axes and parallel to the bedding, were subjected to a total confining stress of 1.5 MPa and a back pressure of 0.3 MPa to initiate the sample saturation process. This effective stress of 1.2 MPa was considered, on one hand, to be sufficiently high to minimise swelling during the re-saturation process and, on the other hand, low enough to allow for testing in lower effective stress regimes at full saturation. After both strains were constant and water uptake was accomplished, the sample was subjected to several checks
115 for the Skempton B-value, i.e. B-checks (Skempton, 1954), by increasing the total confining stress by 0.5 MPa increments under undrained conditions. Once the pore water pressure had equilibrated (typically within 1 hour), the back pressure was raised actively to fulfill B equals 1 to maintain equal effective stresses and associated equal bulk modulus as well as porosity in the saturation phase. To assure complete pore pressure equilibration within the entire sample and to avoid any major consolidation processes, the back-pressure phase lasted around 24 hours. These B-checks have been repeated until the change
120 between two successive B-values was less or equal to 0.05. The complete saturation processes, i.e. initial saturation and B-check phase, lasted around 117 to 148 hours. In the consolidation stage, the confining stress and pore water pressure were increased simultaneously to the desired effective stress over a period of 5 hours. Consolidation was achieved once the backflow

of pore water, as well as changes in axial and radial strains were zero. The complete consolidation process lasted around 45 to 66 hours. In the final shearing stage, the sample was subjected to differential stress by increasing the axial load under undrained conditions. At a constant axial strain rate of $5.0E-07$ 1/s shearing was performed until no differential stress changes occurred and the samples reached the residual effective strength.

2.3 Sample treatment and microstructural analysis

The workflow for the microstructural analysis is presented in Fig. 2. After the tests, the samples were carefully removed from the jackets and dried at room conditions followed by oven-drying at 105°C to constant weight. To maintain the microstructure during further preparation, the samples were subjected to a twofold stabilization by epoxy resin including the all-around surface and the surface cut normal to the shear band. This surface was manually polished using SiC grinding papers and documented by digital photography. Afterwards, sub-samples with sizes of 25 – 350 mm² along the shear zone were prepared for the successive Argon-ion beam polishing using a Leica TiC3X machine. Broad-ion-beam (BIB) polishing was applied for a shorter period of 15 to 30 minutes at 5 kV with an ion beam incident angle of 10.5° and a second period of 4 to 6 hours at 3 kV with an incident angle of 4.5° . The samples were coated by an approximately 7 nm thick layer of tungsten using a Leica ACE600 coating machine. Multiple images were stitched to automatically create larger mosaics using the Aztec software.

SEM-imaging was conducted using a Zeiss SUPRA-55 equipped with SE2- (secondary electron), BSE- (back-scattered electron) and EDS-(energy dispersive X-ray) detectors-, of which the first was used for phase segmentation, i.e., solid material or pore, and the latter two were used for the identification of mineral phases, i.e., heavy or light minerals and chemical composition. The workflow for the microstructural image analysis consisted of producing overview BSE-SEM maps at 100x to 150x magnification, and for a detailed analysis at grain scale, BSE- and SE2-images were taken from regions of interest at various magnifications from 5,000x to 40,000x. Additionally, EDS-element maps were created in combination with BSE-images for a more quantitative determination of mineralogy.

3 Results

3.1 Water content and test configuration

~~Table 1 shows the water content before and after testing. Figure 3 shows the successive Skempton B-values. A complete saturation was assumed when two subsequent B-values differed by ≤ 0.05 . The test configurations and experimental results are summarised in table 2.~~

3.21 Hydromechanical behaviour

~~Table 1 shows the water content before and after testing and figure 3 shows the successive Skempton B-values indicating complete saturation according to the above-defined criteria. The test configurations and experimental results are summarised~~

in table 2. A linear-elastic behaviour was only observed in the very low differential stress region due to the early onset of yielding of OPA (Fig. 4). The results show an increasing Young's modulus and a decreasing Poisson's ratio with increasing effective confining stress (Tab. 2). We define the transition from elasticity to plasticity, i.e. the irreversible, permanent strain, as the onset of yielding determined by the shear stress at which the axial stress-strain curve deviates from linearity (Brace et al., 1966). Yielding, peak and residual stresses increased with increasing effective confining stresses (Tab. 2, Fig. 4). The axial strain at which peak strength was reached increased with effective consolidation stress from 0.44 to 1.11%. All tests showed a strain softening behaviour in the post-peak region. The residual effective strength was established after 1.5 to 2.5 % axial strain indicated by only minor stress or pore pressure changes in the range of 0.01 MPa/h.

The complete effective stress paths for all experiments are presented in Figure 5. We infer volumetric net dilation of the sample from the pore pressure peak during the shearing phase. The onset of net dilation (Tab. 2) took place before peak stress was reached indicating dilation before failure. Both peak and residual strength values showed a non-linear increase with mean effective stress (Fig. 5). A particular difference between the tests at different effective confining stresses was the pore pressure response in the post-peak region. For lower effective confinement ($\sigma'_c = 2.5 - 4$ MPa), the post-failure pore pressure approached its initial consolidation pore pressure, i.e., approaching the theoretical drained stress path (grey lines in Fig. 5). For higher effective confinements ($\sigma'_c = 10 - 16$ MPa) the residual pore pressure was 33 % ($\sigma'_c = 10$ MPa) and 61 % ($\sigma'_c = 16$ MPa) higher than the initial consolidation pore pressure.

3.23 Deformation microstructures

The macro-structural analysis of the sample deformed at 2.5 MPa effective confining stress showed a deformation pattern expressed by multiple sub-parallel shear fractures distributed within the sample. The samples tested at effective confining stresses of 4 MPa or higher revealed multiple shear fractures, which concentrated in form of a central shear band crossing the entire sample (Fig. 6). The macroscopic shear band width was variable across each sample and increases slightly with increasing effective confinement up to widths of 2 mm. The inclination of shear fractures or the shear bands decreased from 70° to 63.5° with increasing effective confinement.

On the mesoscale, i.e., at the mm to hundreds of μm -scale, the macroscopic shear bands consist of a network of multiple shear fractures (Fig. 6a, b). For all specimens, a larger, continuous main fracture was observed, which was accompanied by surrounding parallel and sub-parallel fractures. The amount of these accompanying shear fractures decreases for higher effective consolidation stresses. Fractures at this scale cross the bedding at angles, which are equal to the inclination of the macroscopic shear band. Locally, relative shear displacements were identified, where fractures cross elongated calcite grains oriented sub-parallel or normal to the shear direction resulting in kinking of these elongated components (Fig. 2c, d).

On the grain scale, the microstructure in the vicinity of the macroscopic shear bands was characterised by bands of localised deformation, i.e., shear zones. In these shear zones, the grain orientation changed compared to the non-sheared host rock from less preferred to highly preferred orientations parallel to the macroscopic shear band with increasing effective stresses. Within

185 these zones, crushed or strained fossil shells and fibroidal pyrite aggregates were frequently observed. The intensity of straining and crushing increased with increasing effective confining stress (compare Fig. 7 and Fig. 8).

At low effective confinements, no consistent preferred grain orientation was observed, except for occasional encounters of 1-2 μm -thin layers constituting the shear zone boundary (Y-shears, cf. Logan et al., 1979). Further, the shear zone was comprised of disrupted and loosened grains as well as microlithons with a size of up to 50 μm . Transgranular fractures formed in quartz, 190 calcite, mica and siderite grains inside the shear zone. A pronounced feature exclusively observed in the sample at low effective confinement ($\sigma'_c = 2.5$ MPa) was kink banding (Fig. 7a, a'). Inside these bands, the grain orientation changed the direction by up to 90° along a sharp border. Kink bands were also present as Ca-bearing veins revealed by EDS images (Fig. 7b, b'), which formed buckles oriented in direction of the minimum principal stress.

At 4 and 10 MPa effective confinement, the shear zones showed internal bands of preferred grain orientation parallel to the 195 microscopic and macroscopic shear zone orientation (Fig. 9 for $\sigma'_c = 4$ MPa). Distinct observations were made for the orientation of elongated grains and pores: outside the shear zone, grains and pores are oriented parallel to the macroscopic bedding and the direction of the maximum principal stress, respectively (Fig. 9: rose diagrams, black colour). Within the shear zone, both grains and pores showed different orientations spreading approximately 35 – 40°, ~~an~~ but show an average orientation well-aligned with the microscopic and macroscopic orientation of the shear band (Fig. 9: rose diagrams, red colour), and 200 demonstrate the self-similarity of deformation structures across different scales. The shear zone was characterised by internal and “bordering” bands of obliquely(sub-)parallel-oriented grains clay minerals, i.e. Y-shears, and obliquely-oriented grains P-foliation (cf. Logan et al., 1979), with respect to the shear zone boundary (Fig. 10). Open fractures along these bands contained patches of a few μm up to 2 millimetres in size showing slickensides with striations in a normal-to-surface view (Fig. 9c). The apparent porosity in the shear zone was highly increased by voids formed by trans- and intergranular fractures (Fig. 9b).

205 While the shear zone boundary appeared as a sharp transition for lower to intermediate effective stresses, mainly demonstrated by the increased intergranular porosity and the change of preferred grain orientation within the shear zone (Fig. 9). This sharp transition was less pronounced for the sample tested at 16 MPa effective confining stress (Fig. 8c). Here, the shear zone was accompanied by a broader zone of up to 200 μm width, in which the grain orientation rotated continuously until it was aligned parallel to the shear zone orientation. This transition zone hosted larger elongated calcite and mica grains, which were bent 210 towards the shear zone orientation showing a continuous rotation of up to 135°. Calcite grains presented flexural tension fractures, which were filled by clay particles (Fig. 8b). Mica grains were stretched and folded showing an intracrystalline sub-grain sliding and rotation. Ductile stringers were found as heavily folded organic matter particles (Fig. 8b). Within the shear zone, grains were aligned parallel to the macroscopic shear band orientation. Here, single hard grains such as quartz were mainly intact but partly also transgranular shear fractures were observed (Fig. 8c). The visible shear zone porosity was less 215 increased compared to those in the samples at lower effective stresses.

4 Discussion

4.1 Poromechanical response

220 All samples showed a bulk deformation behaviour typical for an over-consolidated rock under undrained triaxial compression. As presented in previous studies (Amann et al., 2012; Wild and Amann, 2018a), the onset of yielding, also called ‘onset of
225 dilation’, starts in the early stage of differential loading. Wild and Amann (2018a) showed that the shear stress magnitude at the onset of the inelastic strain response depends on the effective consolidation stress and increases with increasing effective
230 confinement, which was also observed in this study. The high values for the Poisson’s ratio, i.e., 0.62 – 0.74, deviate considerably from 0.5 as expected for perfectly linear isotropic materials. Theoretically, for transversal isotropic elastic material, the Poisson’s ratio perpendicular to the plane of anisotropy can be larger than 0.5 since it is not an independent material parameter. The results are in agreement with similar tests on Opalinus Clay (Minardi et al., 2021). In their study, the Poisson’s ratio was measured for both lateral directions showing on average a higher value normal to bedding compared to parallel to bedding by a factor of 3 resulting in an averaged Poisson’s ratio of 0.4. Braun et al. (2021) have reported similar findings for the Callovo-Oxfordian argillite. This observation can be explained by the structural anisotropy of the shale, which favours to deform more in direction normal to bedding due to the preferred alignment of minerals and pores parallel to the bedding plane. The higher Poisson’s ratio at lower effective confinements indicates more lateral deformation perpendicular to the bedding plane than for higher effective confining stresses.

The peak of pore pressure was reached before the peak stress for all samples tested and a pronounced reduction of pore pressure indicated net dilation before failure. However, the onset of dilation varied for each test. For the specimen at lowest effective confinement ($\sigma'_c = 2.5$ MPa), ~~the maximum pore pressure was reached at axial strain shortly before peak stress for the lowest effective confinement ($\sigma'_c = 2.5$ MPa)~~ compared to axial strain at peak strength. Figure 110a shows the axial strain at the onset of net dilation normalised by the axial strain at failure. In contrast to the onset of yielding, this behaviour shows a non-linearly decreasing trend from 92% to 80 % of axial strain to the axial strain at peak strength with increasing effective confinement. This observation suggests that at high effective confining stresses plastic strain associated with dilation starts earlier compared to low effective confinements, and consequently plastic strain is accumulating for a longer period without complete failure.
240 The magnitude of maximum pore pressure developed under undrained shearing increases in a non-linear fashion (Fig. 101b), which is in agreement with observations made by Wild and Amann 2018a. Furthermore, the effective stress path after failure indicates a less dilatant behaviour for higher effective confinements demonstrated by significantly higher pore water pressures at residual strength state.

4.2 Deformation processes

245 Even though all samples deformed in a brittle manner in terms of their post-failure strain-softening behaviour and their localised deformation within a shear band or shear fractures on the macroscale, there were major differences in deformation characteristics on the microstructural level. Deformation structures and related processes were strongly dependent on the

effective stress. A gradual change has been observed from low effective stresses presenting brittle deformation indicators such as shear fracturing and grain kinking to more ductile processes including inter-particle sliding, and grain bending for higher effective confinements. These observations suggest a transition from brittle-dominated shear failure towards a semi-brittle to ductile shearing on the microscale. Underlying deformation mechanisms in the low effective stress range are cataclasis including the formation of multiple shear fractures characterising the shear zone, while at higher effective stresses, deformation is expressed by grain boundary and rotational sliding forming a ductile shear zone (cf. Ramsay and Huber, 1987). Nonetheless, we emphasise that there is a coexistence of brittle and ductile deformation processes on the grain scale as observed also in other studies (Yongnian et al., 1989; Schuster et al. 2021; Winhausen et al., 2021). This appears to be associated with the contrasting mineral stiffnesses of the constituents such as hard calcite and quartz grains, and softer phyllosilicates. In contrast to the shaly facies of OPA from the MT-URL, the sandy facies is characterised by a heterogeneous mineralogy distribution at the macroscale (Lauper et al., 2021; Kneucker and Furche, 2021) and the microscale (Houben et al., 2014). This heterogeneity is also manifested in the distribution and the style of deformation within this facies (Schuster et al., 2021). However, the shaly facies can be considered homogeneous on the mm-scale (cf. Fig. 6), and deformation processes observed in selected areas of the sub-samples are considered representative for the entire sample, and allow for comparing the structures encountered in all samples of this study.

An additional difference in structural deformation was observed for the porosity within the shear zones. While all samples showed an increased shear zone porosity, we observed a decreasing trend with increasing effective confinements. Furthermore, the shear zone width increases with effective confinement and its boundary changes from a sharp boarder (Fig. 7,9) to a smooth broader transition zone (Fig. 8). These observations are corroborated by the deformation processes analysed above: Localised brittle shear fracturing at low effective stresses facilitates more dilation while ductile shearing suppresses dilation but requires more space for strain accommodation.

These findings are consistent with observations on a suppressed dilation and the reduced magnitude of pore pressure development for higher effective stresses. Furthermore, the earlier dilation before failure at high effective stresses can be related to the formation of the transition zone. The formation of the ~~bent~~ transition zone has been initiated in the pre-failure regime due to fabric rotation and dragging. Once minerals and pores were rotated to a preferred orientation and well-aligned, i.e., to the orientation of the microscopic and macroscopic shear zone/band, bulk failure is initiated. In the post-peak region, most of the shear strain is likely accommodated in the narrow shear zone of preferred mineral orientation, which is in agreement with the slickensides of a considerable size found in the shear zones (Fig. 9c). Here, strongly localised shear strain leads to intercrystalline sliding and eventually to the delamination of phyllosilicates (Fig. 8c).

All samples were sheared to their residual strength where the effective stress remained essentially constant. Thus, we conclude that further straining may not cause structural or void changes, i.e., a critical state. During further shearing, we infer that deformation is accommodated by frictional flow and sliding in the shear zones with preferred mineral orientations, i.e., P-foliations, while the fabric elements remain constant (cf. Haines et al., 2013).

4.2 Effective strength and failure mode

A change in failure mode from axial splitting to shear failure has been inferred from macroscopic observations for OPA from unconfined up to confinements of 4 MPa (Amann et al., 2011; Amann et al., 2012). In this study, we extend this observation to higher effective confinements, and - based on our microstructural analysis - we are able to transfer the bulk geomechanical behaviour to the processes on the microscale level.

The transitional change of failure mode on the microscale correlates well with the bulk failure behaviour. The non-linear changes of stiffness, onset of dilation, dilation magnitude, as well as peak and residual strength with effective stresses are governed by the changing micromechanical processes. For the peak and residual strength, the non-linear failure envelope implies a change in friction angle with increasing effective confinement, which is likely associated with the gradual change in shear band inclination and the transition from brittle to ductile-dominated deformation. At lower effective stresses, micro-cracking and multiple shear fracturing require more shear stress to overcome higher internal frictional resistances compared to intergranular grain boundary sliding and bending at higher effective stresses.

The decrease in friction angle due to an increase in ductility has also been demonstrated experimentally for saturated kaolinite and bentonite clays (Hicher et al., 2000). For the case of clay-rich rocks such as shales, Niandou et al. (1997) have shown that the failure surface of Tournemire Shale is non-linear and the failure mode depends on the confining stress.

To constrain a failure criterion for peak and residual strength, we combine our results with those of Wild and Amann 2018a (Fig. 12). As opposed to the linear and bi-linear failure criteria established in past studies for OPA (Amann et al., 2012; Favero et al. 2018; Minardi et al., 2021; Wild and Amann, 2018a), we propose a non-linear envelope for the ultimate and residual strength as derived for other clays (e.g., Bishop et al., 1965; Petley, 1999). Therefore, we use the modified constitutive equation (Eq. 1) to describe the failure surface in 2D q - p' -space proposed for geologic materials by Desai et al. (1984). To fit this model to the data presented in Figure 5, the parameters shown in Table 3 were used, where q is the differential stress at peak and residual strength in MPa, respectively, p' is the mean effective stress in MPa, and μ , C and β are fitting parameters.

$$q = (\mu p' + C)e^{-\beta p'} \quad \text{Eq. 1}$$

4.3 Implication for the storage of radioactive waste

For the application as a host rock for nuclear waste, the findings on the hydromechanical and deformation behaviour of Opalinus Clay can be transferred to predict the in-situ behaviour of the rock mass. During the construction of the repository, excavation-induced damage in Opalinus Clay and other clay-rich rocks considered as potential host rocks, has been reported in many studies (e.g. Bossart et al. 2002; Nussbaum et al. 2011; Lanyon et al., 2015; Yong et al. 2017). However, studies focusing on the structures developed in response to induced stress changes, were limited to macro- and mesoscale observations differentiating between shear and extensional fractures (Labiouse and Vietor, 2014; Armand et al., 2014; Kupferschmied et al., 2015). This study provides insight into the deformation behaviour and processes on the microscale, which differ depending

315 on the mean effective stress. Hence, the expression of excavation-induced damage likely changes with distance from the tunnel as mean stresses change. In particular, at low effective stresses, changes in permeability are more likely to emerge due to the more dilatant behaviour and the increased shear zone porosity. Remaining questions arise, if the deformation behaviour observed also applies to long-term deformation associated with creep, and elevated temperature developing after waste storage. The latter might cause changes in mineralogy, particularly in the clay mineralogy, which can lead to hydromechanical changes in the physical behaviour of the rock.

5 Summary and conclusions

320 In consolidated undrained triaxial compression, Opalinus Clay shows a transitional failure behaviour from brittle- to ductile-dominated deformation with increasing effective confining stress. Although in a classical sense, the general bulk behaviour can be described as brittle deformation due to the early failure ($< 1.5 \epsilon_{ax}$), the strain-softening behaviour in the post-peak phase, and the localised strain in distinct shear bands, our results suggest these indicators are insufficient for properly describing the failure mechanism. Instead, we highlight the significance of micro-mechanical processes in the microscale governing the failure mode and controlling the rheology of the material.

325 Our results demonstrate the transition in failure mode by, firstly, the non-linear dependency of hydro-mechanical properties on effective stress, i.e., the onset of net dilation, the magnitude of developed pore pressure, as well as peak and residual strength, and, secondly, the structural deformation processes changing from brittle-dominated to ductile-dominated failure on the microscale. This transition is accompanied by a decreasing porosity in the shear zone and a less pronounced dilation with increasing effective confining stresses. Our conceptual microstructural model (Fig. 124) for shear failure in Opalinus Clay is characterised by a set of multiple, distinct and dilatant shear zones with brittle-dominated deformation for lower effective stresses in the range of 2.5 MPa effective stress at failure. For effective stresses around 4 to 10 MPa, OPA shows a transitional failure mode. For effective confining stresses in the range of 16 MPa and expectedly higher stresses, failure on the microscale is a less dilatant forming a broader shear zone dominated by ductile deformation. Based on these observations, we propose a non-linear failure criterion to describe the behaviour of shaly Opalinus Clay.

Data availability. Lab testing data and high-resolution BIB-SEM images are available in the supplement provided.

Competing interests. The authors declare that they have no conflict of interest.

340 *Author contributions.* LW performed the laboratory tests, BIB-SEM microscopy, data analysis, and wrote the manuscript with contributions from all authors. LW, KK, MRJ and JLU discussed the results. FA acquired funding and contributed to the interpretation of the results.

Acknowledgements. We would like to thank the Swiss Federal Nuclear Safety Inspectorate (ENSI) for funding this work, which was performed within the framework of the project entitled “Development and Validation of a Constitutive Model for Opalinus

345 Clay". We thank the two reviewers, Tom Blenkinshop and Mike Chandler, for their constructive comments, which improved the manuscript.

350 **6 References**

Amann, F., Button, E. A., Evans, K. F., Gischig, V. S., and Blümel, M.: Experimental Study of the Brittle Behavior of Clay shale in Rapid Unconfined Compression, Rock Mechanics and Rock Engineering, 44, 415–430, <https://doi.org/10.1007/s00603-011-0156-3>, 2011.

355 Amann, F., Kaiser, P., and Button, E. A.: Experimental Study of Brittle Behavior of Clay Shale in Rapid Triaxial Compression, Rock Mechanics and Rock Engineering, 45, 21–33, <https://doi.org/10.1007/s00603-011-0195-9>, 2012.

Armand, G., Leveau, F., Nussbaum, C., de La Vaissiere, R., Noiret, A., Jaeggi, D., Landrein, P. and Righini, C.: Geometry and properties of the excavation-induced fractures at the Meuse/Haute-Marne URL drifts. Rock mechanics and rock engineering, 47(1), pp.21-41, <https://doi.org/10.1007/s00603-012-0339-6>, 2014.

360 Attewell, P. B. and Sandford, M. R.: Intrinsic Shear Strength of a Brittle, Anisotropic Rock — I: Experimental and Mechanical Interpretation, International Journal of Rock Mechanics and Mining Sciences & Geomechanics Abstracts, 11, 423-430, 1974.

Bésuelle, P., Viggiani, G., Desrues, J., Coll, C., and Charrier, P.: A Laboratory Experimental Study of the Hydromechanical Behavior of Boom Clay, Rock Mechanics and Rock Engineering, 47, 143–155, <https://doi.org/10.1007/s00603-013-0421-8>, 2014.

365 Bishop, A. W., Webb, D. L., and Lewin, P. I.: Undisturbed Samples of London Clay from the Ashford Common Shaft: Strength–Effective Stress Relationships, Géotechnique, 15, 1–31, <https://doi.org/10.1680/geot.1965.15.1.1>, 1965.

Bossart, P., Meier, P.M., Moeri, A., Trick, T. and Mayor, J.C.: Geological and hydraulic characterisation of the excavation disturbed zone in the Opalinus Clay of the Mont Terri Rock Laboratory. Engineering Geology, 66(1-2), pp.19-38, [https://doi.org/10.1016/S0013-7952\(01\)00140-5](https://doi.org/10.1016/S0013-7952(01)00140-5), 2002.

370 Brace, W. F., Paulding, B. W., and Scholz, C.: Dilatancy in the fracture of crystalline rocks, Journal of Geophysical Research, 71(16), 3939–3953, <https://doi.org/10.1029/JZ071i016p03939>, 1966.

Braun, P., Ghabezloo, S., Delage, P., Sulem, J. and Conil, N.: Transversely isotropic poroelastic behaviour of the Callovo-Oxfordian claystone: A set of stress-dependent parameters. Rock Mechanics and Rock Engineering, 54(1), pp.377-396, <https://doi.org/10.1007/s00603-020-02268-z>, 2021.

- 375 Braun, P., Ghabezloo, S., Delage, P., Sulem, J., and Conil, N.: Transversely Isotropic Poroelastic Behaviour of the Callovo-Oxfordian Claystone: A Set of Stress-Dependent Parameters, *Rock Mech Rock Eng.*, 54, 377–396, <https://doi.org/10.1007/s00603-020-02268-z>, 2021.
- Byerlee, J.D.: Brittle-ductile transition in rocks. *Journal of Geophysical Research*, 73(14), pp.4741-4750, <https://doi.org/10.1029/JB073i014p04741>, 1968.
- 380 Delage, P. and Tessier, D.: Macroscopic effects of nano and microscopic phenomena in clayey soils and clay rocks, *Geomechanics for Energy and the Environment*, 27, 100177, <https://doi.org/10.1016/j.gete.2019.100177>, 2021.
- Desai, C. S., and Siriwardane, H. J.: Constitutive laws for engineering materials, with emphasis on geologic materials. Prentice Hall, 468pp, 1984.
- Desbois, G., Höhne, N., Urai, J. L., Bésuelle, P., and Viggiani, G.: Deformation in cemented mudrock (Callovo–
385 Oxfordian Clay) by microcracking, granular flow and phyllosilicate plasticity: insights from triaxial deformation, broad ion beam polishing and scanning electron microscopy, *Solid Earth*, 8, 291–305, <https://doi.org/10.5194/se-8-291-2017>, 2017.
- Djéran-Maigre, I., Tessier, D., Grunberger, D., Velde, B., and Vasseur, G.: Evolution of microstructures and of macroscopic properties of some clays during experimental compaction, *Marine and Petroleum Geology*, 15, 109–128, [https://doi.org/10.1016/S0264-8172\(97\)00062-7](https://doi.org/10.1016/S0264-8172(97)00062-7), 1998.
- 390 Evans, B., Fredrich, J. T., and Wong, T.: The brittle-ductile transition in rocks: Recent experimental and theoretical progress, in: *Geophysical Monograph Series*, vol. 56, edited by: Duba, A. G., Durham, W. B., Handin, J. W., and Wang, H. F., American Geophysical Union, Washington, D. C., 1–20, <https://doi.org/10.1029/GM056p0001>, 1990.
- Favero, V., Ferrari, A., and Laloui, L.: Anisotropic Behaviour of Opalinus Clay Through Consolidated and Drained Triaxial Testing in Saturated Conditions, 51, 1305–1319, <https://doi.org/10.1007/s00603-017-1398-5>, 2018.
- 395 Goetze, C.: High temperature rheology of westerly granite, *J. Geophys. Res.*, 76, 1223–1230, <https://doi.org/10.1029/JB076i005p01223>, 1971.
- Gramberg, J.: The axial cleavage fracture 1 Axial cleavage fracturing, a significant process in mining and geology. *Engineering Geology*, 1(1), 31-72, [https://doi.org/10.1016/0013-7952\(65\)90006-2](https://doi.org/10.1016/0013-7952(65)90006-2), 1965
- Griggs, D., and Handin, J.: Observations on fracture and a hypothesis of earthquakes. book chapter in *Rock Deformation (A Symposium)* by Griggs, D. and Handin, J., 79, <https://doi.org/10.1130/MEM79>, 1960.
- 400 Haines, S. H., Kaproth, B., Marone, C., Saffer, D., and van der Pluijm, B.: Shear zones in clay-rich fault gouge: A laboratory study of fabric development and evolution, *Journal of Structural Geology*, 51, 206–225, <https://doi.org/10.1016/j.jsg.2013.01.002>, 2013.
- Handin, J., Hager Jr, R.V., Friedman, M. and Feather, J.N.: Experimental deformation of sedimentary rocks under
405 confining pressure: pore pressure tests. *AAPG Bulletin*, 47(5), pp.717-755, 1963.
- Hattab, M. and Fleureau, J.-M.: Experimental analysis of kaolinite particle orientation during triaxial path, *Int. J. Numer. Anal. Meth. Geomech.*, 35, 947–968, <https://doi.org/10.1002/nag.936>, 2011.

- Hattab, M., Hammad, T., Fleureau, J.-M., and Hicher, P.-Y.: Behaviour of a sensitive marine sediment: microstructural investigation, *Géotechnique*, 63, 71–84, <https://doi.org/10.1680/geot.10.P.104>, 2013.
- 410 Heard, H. C.: Transition from brittle fracture to ductile flow in Solenhofen limestone as a function of temperature, confining pressure, and interstitial fluid pressure, book chapter in Rock Deformation (A Symposium) by Griggs, D. and Handin, J., 79, <https://doi.org/10.1130/MEM79-p193>, 1960.
- Hicher, P. Y., Wahyudi, H., and Tessier, D.: Microstructural analysis of inherent and induced anisotropy in clay, *Mech. Cohes.-Frict. Mater.*, 5, 341–371, 2000.
- 415 Houben, M. E., Desbois, G., and Urai, J. L.: A comparative study of representative 2D microstructures in Shaly and Sandy facies of Opalinus Clay (Mont Terri, Switzerland) inferred from BIB-SEM and MIP methods, 49, 143–161, <https://doi.org/10.1016/j.marpetgeo.2013.10.009>, 2014.
- Ibanez, W. D. and Kronenberg, A. K.: Experimental deformation of shale: Mechanical properties and microstructural indicators of mechanisms, 30, 723–734, [https://doi.org/10.1016/0148-9062\(93\)90014-5](https://doi.org/10.1016/0148-9062(93)90014-5), 1993.
- 420 Ingram, G. M. and Urai, J. L.: Top-seal leakage through faults and fractures: the role of mudrock properties, 158(1), 125–135, <https://doi.org/10.1144/GSL.SP.1999.158.01.10>, 1999.
- Klinkenberg, M., Kaufhold, S., Dohrmann, R., and Siegesmund, S.: Influence of carbonate microfabrics on the failure strength of claystones, 107, 42–54, <https://doi.org/10.1016/j.enggeo.2009.04.001>, 2009.
- Kneuker, T. and Furche, M.: Capturing the structural and compositional variability of Opalinus Clay: constraints from multidisciplinary investigations of Mont Terri drill cores (Switzerland), *Environ Earth Sci*, 80, 421, <https://doi.org/10.1007/s12665-021-09708-1>, 2021.
- 425 Kranz, R. L.: Microcracks in rocks: A review, *Tectonophysics*, 100, 449–480, [https://doi.org/10.1016/0040-1951\(83\)90198-1](https://doi.org/10.1016/0040-1951(83)90198-1), 1983.
- Kupferschmid, N., Wild, K.M., Amann, F., Nussbaum, C., Jaeggi, D. and Badertscher, N.: Time-dependent fracture formation around a borehole in a clay shale. *International Journal of Rock Mechanics and Mining Sciences*, 77, pp.105-114, <https://doi.org/10.1016/j.ijrmms.2015.03.027>, 2015.
- 430 Labieuse, V. and Vietor, T.: Laboratory and in situ simulation tests of the excavation damaged zone around galleries in Opalinus Clay. *Rock Mechanics and Rock Engineering*, 47(1), pp.57-70, <https://doi.org/10.1007/s00603-013-0389-4>, 2014.
- Lanyon, G.W., Martin, D., Giger, S. and Marschall, P.: Development and evolution of the Excavation Damage Zone (EDZ) in the Opalinus Clay – A synopsis of the state of knowledge from Mont Terri, NAGRA Arbeitsbericht NAB 14-87, 2014.
- 435 Lauper, B., Zimmerli, G. N., Jaeggi, D., Deplazes, G., Wohlwend, S., Rempfer, J., and Foubert, A.: Quantification of Lithological Heterogeneity Within Opalinus Clay: Toward a Uniform Subfacies Classification Scheme Using a Novel Automated Core Image Recognition Tool, *Front. Earth Sci.*, 9, 645596, <https://doi.org/10.3389/feart.2021.645596>, 2021.
- 440 Logan, J. M., Friedman, M., Dengo, C., Shimamoto, T., and Higgs, N.: Experimental studies of simulated gouge and their application to studies of natural fault zones, 39, 1979.

- Mäder, U.: Recipe and preparation of a simplified artificial pore water for Opalinus Clay and “Brown Dogger” based on the Nagra reference pore water composition, containing Na- K-Ca-Mg-Cl-SO₄-HCO₃, and adjusted to atmospheric PCO₂. *NAGRA AN*, 11-159, 2011.
- 445 Menéndez, B., Zhu, W., and Wong, T.-F.: Micromechanics of brittle faulting and cataclastic flow in Berea sandstone. *Journal of Structural Geology*, 18, 1–16, [https://doi.org/10.1016/0191-8141\(95\)00076-P](https://doi.org/10.1016/0191-8141(95)00076-P), 1996.
- Minardi, A., Giger, S. B., Ewy, R. T., Stankovic, R., Stenebråten, J., Soldal, M., Rosone, M., Ferrari, A., and Laloui, L.: Benchmark study of undrained triaxial testing of Opalinus Clay shale: Results and implications for robust testing. *Geomechanics for Energy and the Environment*, 25, 100210, <https://doi.org/10.1016/j.gete.2020.100210>, 2021.
- 450 Mogi, K.: Pressure Dependence of Rock Strength and Transition from Brittle Fracture to Ductile Flow, *Bulletin of the Earthquake Research Institute*, 44, 215-232, 1966.
- Morgenstern, N. R. and Tchalenko, J. S.: Microscopic structures in kaolin subjected to direct shear, *Geotechnique*, 17, 309-328, <https://doi.org/10.1680/geot.1967.17.4.309>, 1967.
- 455 Niandou, H., Shao, J. F., Henry, J. P., and Fourmaintraux, D.: Laboratory Investigation of the Mechanical Behaviour of Tournemire Shale, *Int. J. Rock Mech. Min. Sci.*, 34(1), 3-16, [https://doi.org/10.1016/S1365-1609\(97\)80029-9](https://doi.org/10.1016/S1365-1609(97)80029-9), 1997.
- Nussbaum, C., Bossart, P., Amann, F. and Aubourg, C.: Analysis of tectonic structures and excavation induced fractures in the Opalinus Clay, Mont Terri underground rock laboratory (Switzerland). *Swiss Journal of Geosciences*, 104(2), pp.187-210. , <https://doi.org/10.1007/s00015-011-0070-4>, 2011.
- 460 Nygård, R., Gutierrez, M., Bratli, R. K., and Høeg, K.: Brittle–ductile transition, shear failure and leakage in shales and mudrocks, *Marine and Petroleum Geology*, 23(2), 201–212, <https://doi.org/10.1016/j.marpetgeo.2005.10.001>, 2006.
- Oelker, Anne. Deformation properties of Boom Clay: Implementation of a multi-scale concept. No. RWTH-2019-09913. PhD Thesis, published at RWTH Publications, 2020.
- Ramsay, J.G., Huber, M.I. and Lisle, R.J.: The techniques of modern structural geology: Folds and fractures (Vol. 2). Academic press, 1983.
- 465 Petley, D. N.: Failure envelopes of mudrocks at high confining pressures, Geological Society, London, Special Publications, 158, 61–71, <https://doi.org/10.1144/GSL.SP.1999.158.01.05>, 1999.
- Rutter, E.H.: On the nomenclature of mode of failure transitions in rocks. *Tectonophysics*, 122(3-4), pp.381-387, [https://doi.org/10.1016/0040-1951\(86\)90153-8](https://doi.org/10.1016/0040-1951(86)90153-8), 1986.
- 470 Sarout, J., Esteban, L., Delle Piane, C., Maney, B., and Dewhurst, D. N.: Elastic anisotropy of Opalinus Clay under variable saturation and triaxial stress, *Geophysical Journal International*, 198(3), 1662–1682, <https://doi.org/10.1093/gji/ggu231>, 2014.
- Schuck, B., Desbois, G., and Urai, J. L.: Grain-scale deformation mechanisms and evolution of porosity in experimentally deformed Boom Clay, *Journal of Structural Geology*, 130, 103894, <https://doi.org/10.1016/j.jsg.2019.103894>, 2020.

- 475 Schuster, V., Rybacki, E., Bonnelye, A., Herrmann, J., Schleicher, A. M., and Dresen, G.: Experimental Deformation of Opalinus Clay at Elevated Temperature and Pressure Conditions: Mechanical Properties and the Influence of Rock Fabric. Rock Mech Rock Eng, <https://doi.org/10.1007/s00603-021-02474-3>, 2021.
- Sellin, P. and Leupin, O. X.: The Use of Clay as an Engineered Barrier in Radioactive-Waste Management – A Review. Clays and Clay Minerals, 61(6), 477–498, <https://doi.org/10.1346/CCMN.2013.0610601>, 2013.
- Skempton, A. W.: Some observations on tectonic shear zones, 1st ISRM Congress, 1966.
- 480 Skempton, A. W.: The pore-pressure coefficients A and B, Géotechnique, 4, 143–147, <https://doi.org/10.1680/geot.1954.4.4.143>, 1954.
- Tchalenko, J. S.: Similarities between Shear Zones of Different Magnitudes, Geol Soc America Bull, 81(6), 1625-1640, [https://doi.org/10.1130/0016-7606\(1970\)81\[1625:SBSZOD\]2.0.CO;2](https://doi.org/10.1130/0016-7606(1970)81[1625:SBSZOD]2.0.CO;2), 1970.
- Tchalenko, J. S.: The evolution of kink-bands and the development of compression textures in sheared clays, Tectonophysics, 6, 159–174, [https://doi.org/10.1016/0040-1951\(68\)90017-6](https://doi.org/10.1016/0040-1951(68)90017-6), 1968.
- 485 Thury, M. and Bossart, P.: The Mont Terri rock laboratory, a new international research project in a Mesozoic shale formation, in Switzerland, Engineering Geology, 52, 347–359, [https://doi.org/10.1016/S0013-7952\(99\)00015-0](https://doi.org/10.1016/S0013-7952(99)00015-0), 1999.
- Wild, K. M. and Amann, F.: Experimental study of the hydro-mechanical response of Opalinus Clay – Part 1: Pore pressure response and effective geomechanical properties under consideration of confinement and anisotropy, Engineering
- 490 Geology, 237, 32–41, <https://doi.org/10.1016/j.enggeo.2018.02.012>, 2018.
- Wild, K. M. and Amann, F.: Experimental study of the hydro-mechanical response of Opalinus Clay – Part 2: Influence of the stress path on the pore pressure response, Engineering Geology, 237, 92–101, <https://doi.org/10.1016/j.enggeo.2018.02.011>, 2018.
- Winhausen, L., Klaver, J., Schmatz, J., Desbois, G., Urai, J. L., Amann, F., and Nussbaum, C.: Micromechanisms leading to shear failure of Opalinus Clay in a triaxial test: a high-resolution BIB–SEM study, Solid Earth, 12, 2109–2126, <https://doi.org/10.5194/se-12-2109-2021>, 2021.
- 495 Wong, T., David, C., and Zhu, W.: The transition from brittle faulting to cataclastic flow in porous sandstones: Mechanical deformation, J. Geophys. Res., 102, 3009–3025, <https://doi.org/10.1029/96JB03281>, 1997.
- Yong, S., Loew, S., Schuster, K., Nussbaum, C. and Fidelibus, C.: Characterisation of excavation-induced damage around
- 500 a short test tunnel in the Opalinus Clay. Rock Mechanics and Rock Engineering, 50(8), pp.1959-1985, <https://doi.org/10.1007/s00603-017-1212-4>, 2017.
- Yongnian, H., Chuanyong, L., and Lanbin, S.: Microstructural Features of Deformed Rocks across the Brittle-Ductile Transition, Physics and Chemistry of the Earth, 17, 11-15, [https://doi.org/10.1016/0079-1946\(89\)90003-7](https://doi.org/10.1016/0079-1946(89)90003-7), 1989.

505

7 Figures

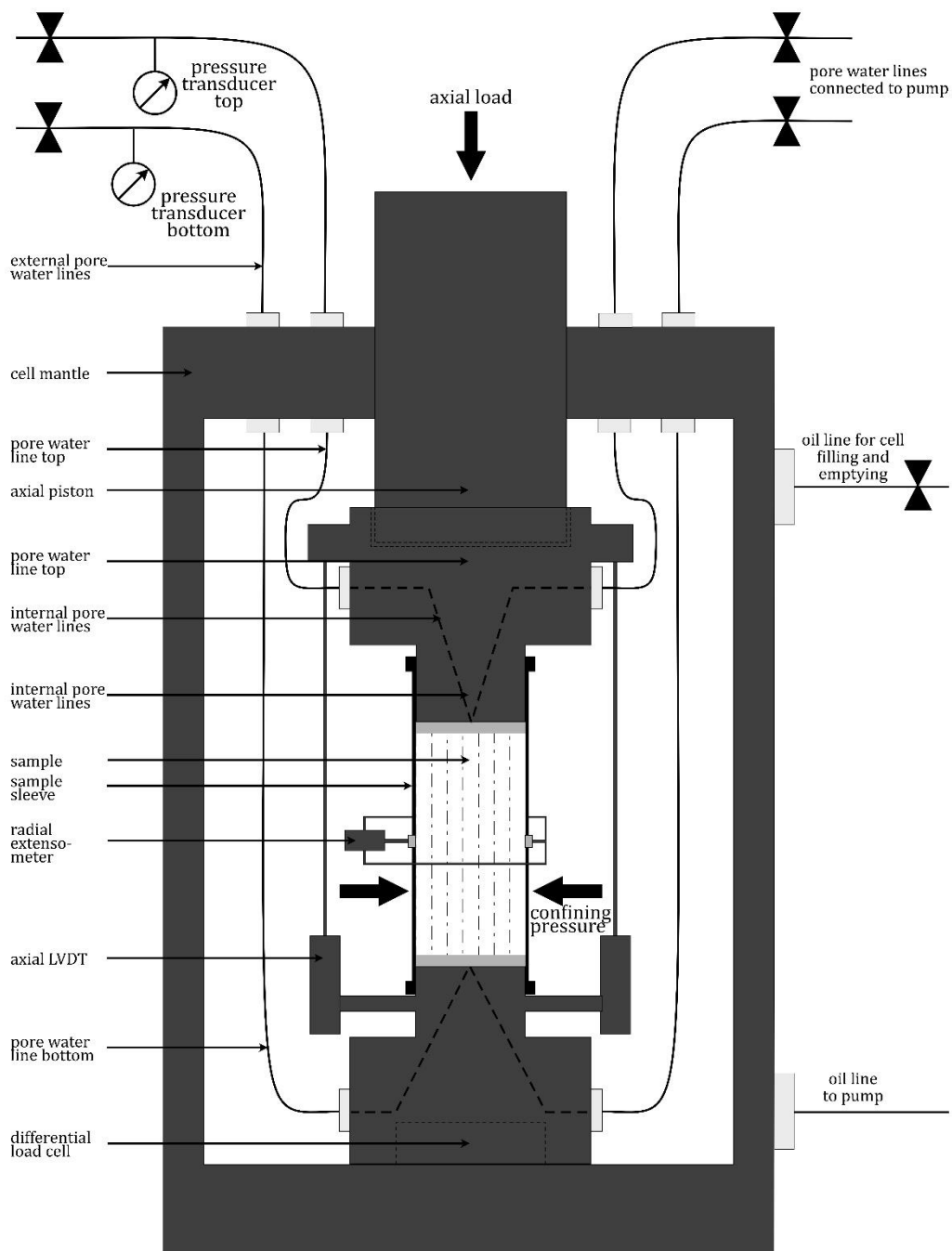


Figure 1: Experimental setup showing the cell configuration and the sensor assemblage.

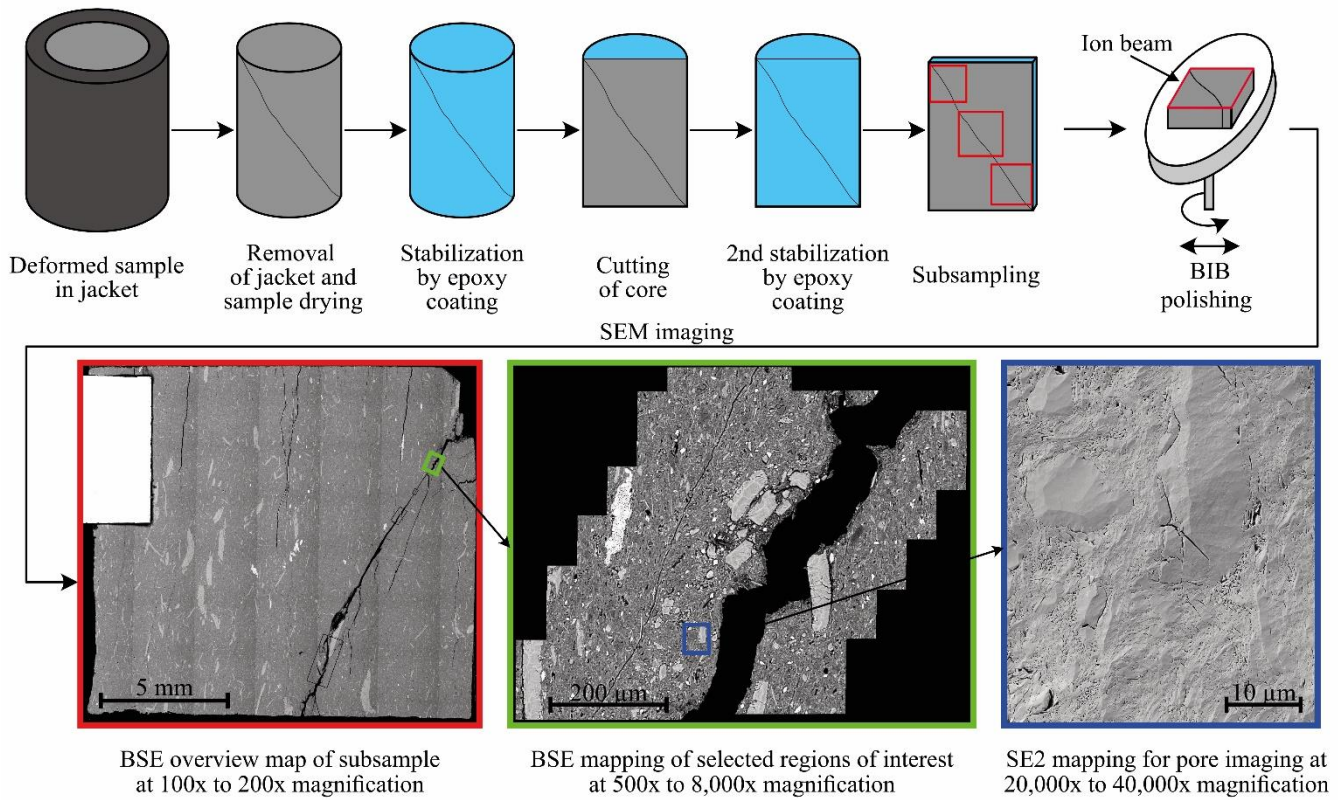
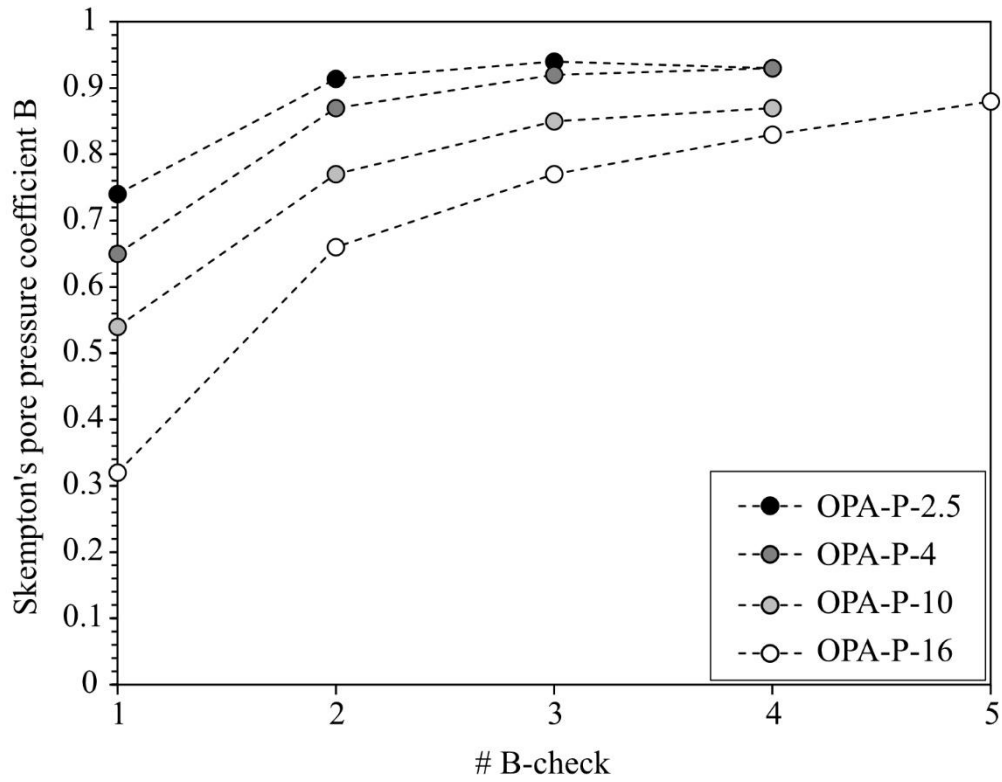
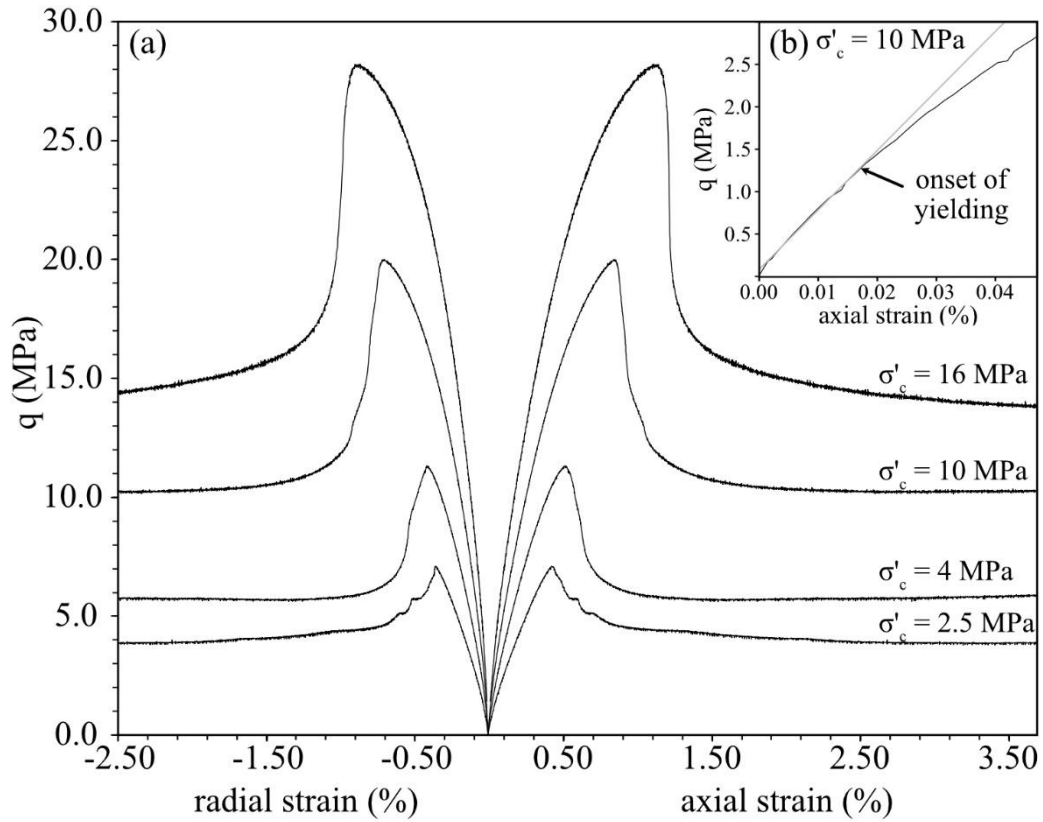


Figure 2: Procedure of sample preparation and workflow for microstructural analysis including the two-fold stabilisation the broad-ion-beam polishing and the imaging strategy.



515

Figure 3: Skempton B-values demonstration the saturation of the samples. Experiments are numbered according to the sequence of performance with increasing effective consolidation stresses used, i.e. 2.5, 4, 10 and 16 MPa.



520 **Figure 4: (a) Differential stress-strain curves of all tests, where as radial strain in measured normal to the bedding plane. (b) shows the early linear-elastic strain region for test OPA-P-10. The linear fit (grey line) is used to constrain the elastic parameters and the deviation from linearity, i.e. on the onset of yielding.**

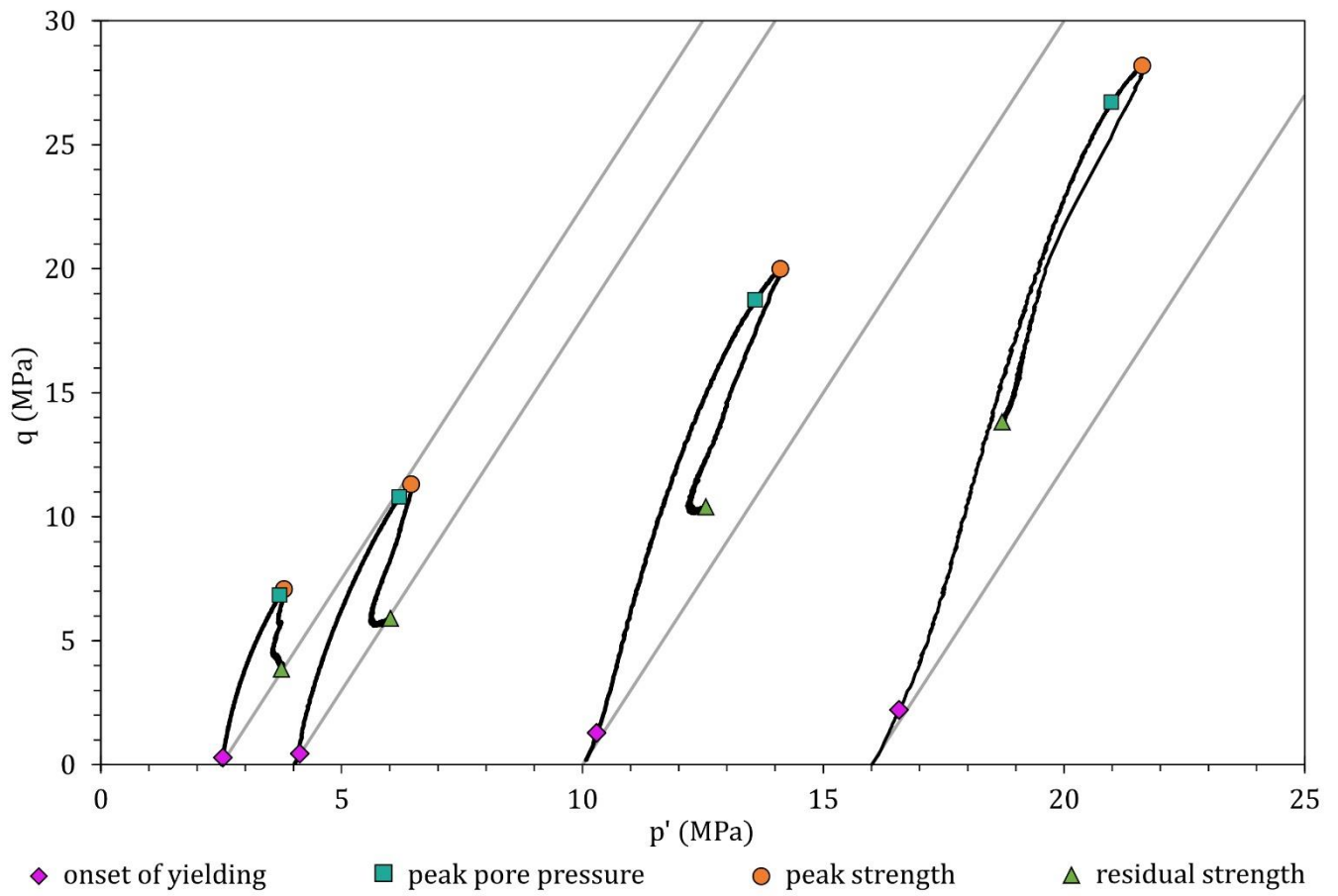
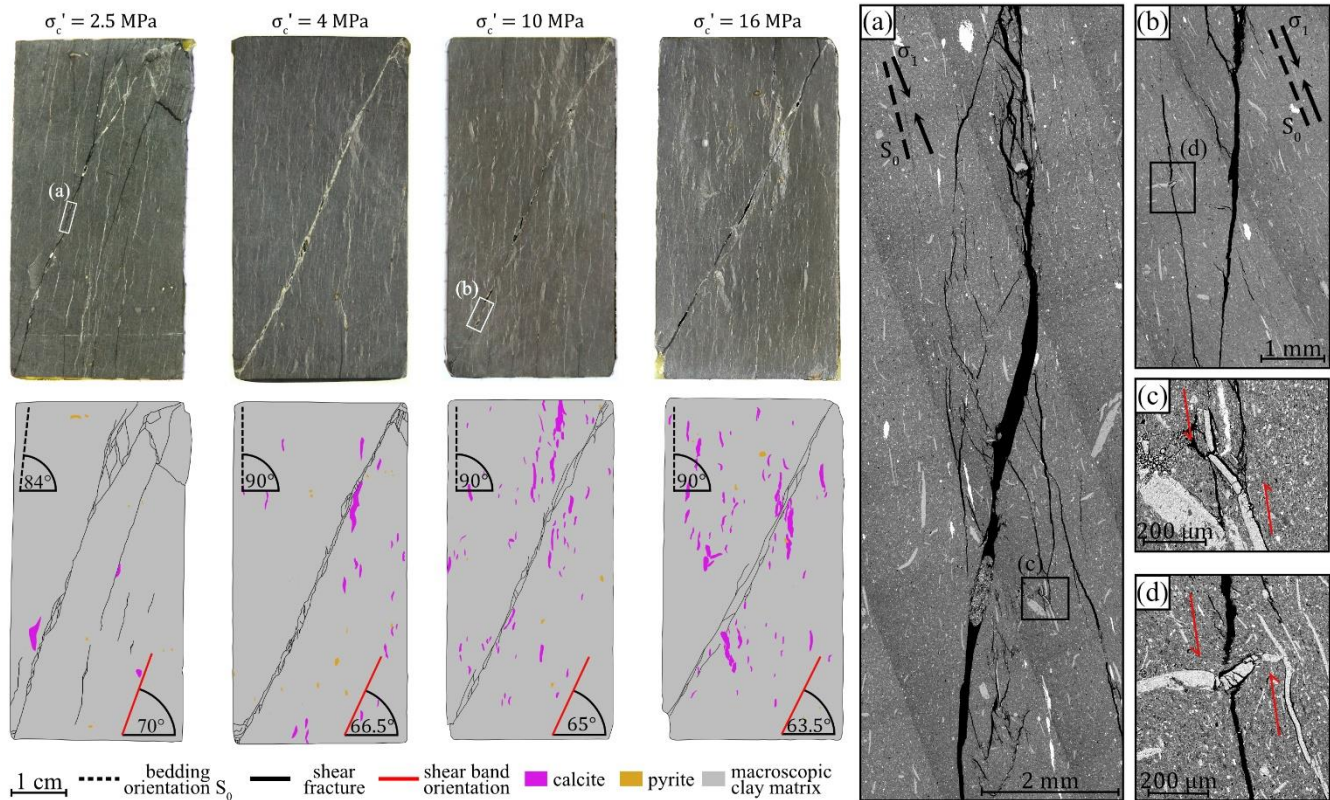


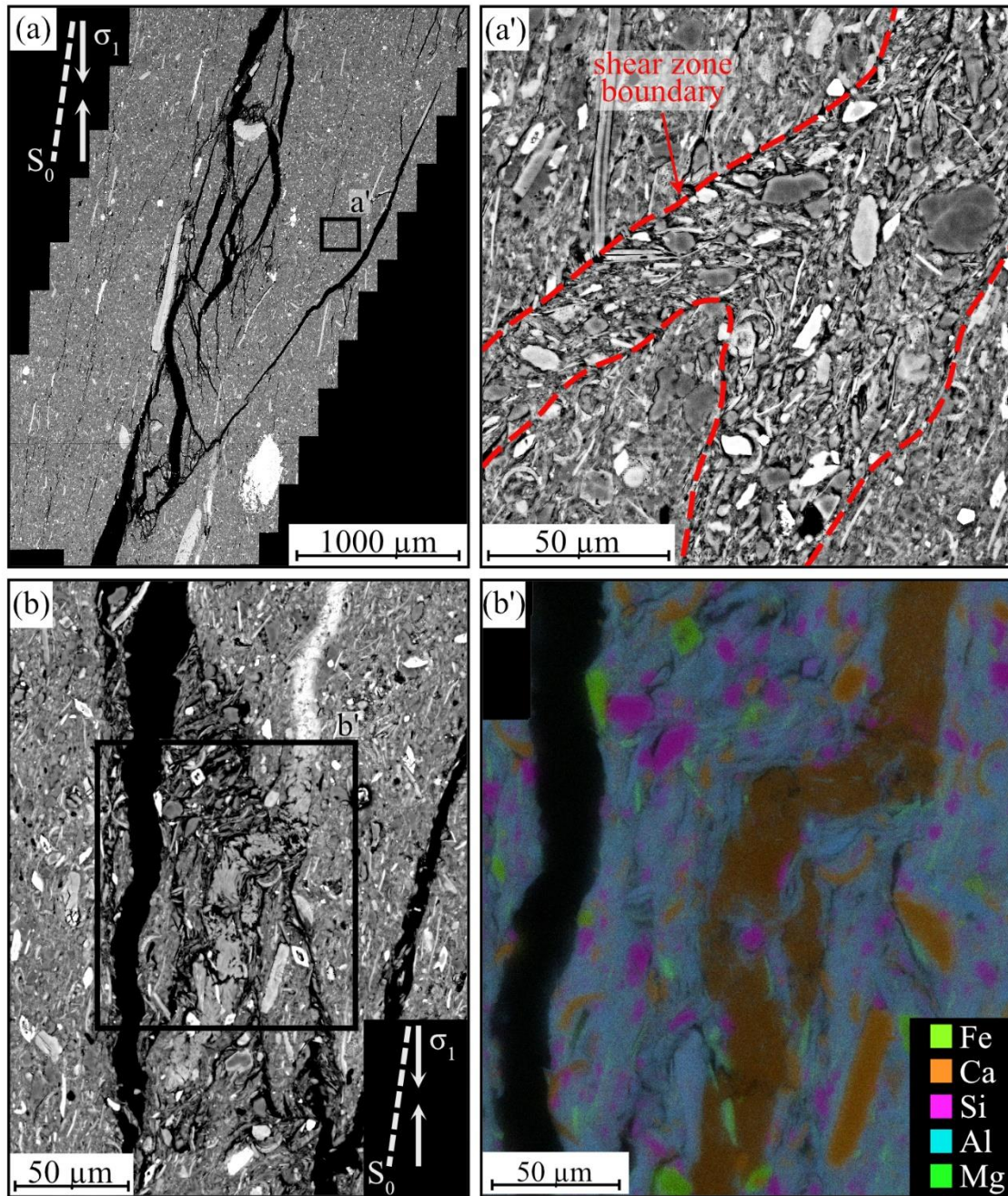
Figure 5: Effective stress paths for samples with consolidation stresses 2.5, 4, 10 and 16 MPa. The grey lines represent the theoretical drained stress path, i.e., constant pore pressures.

525

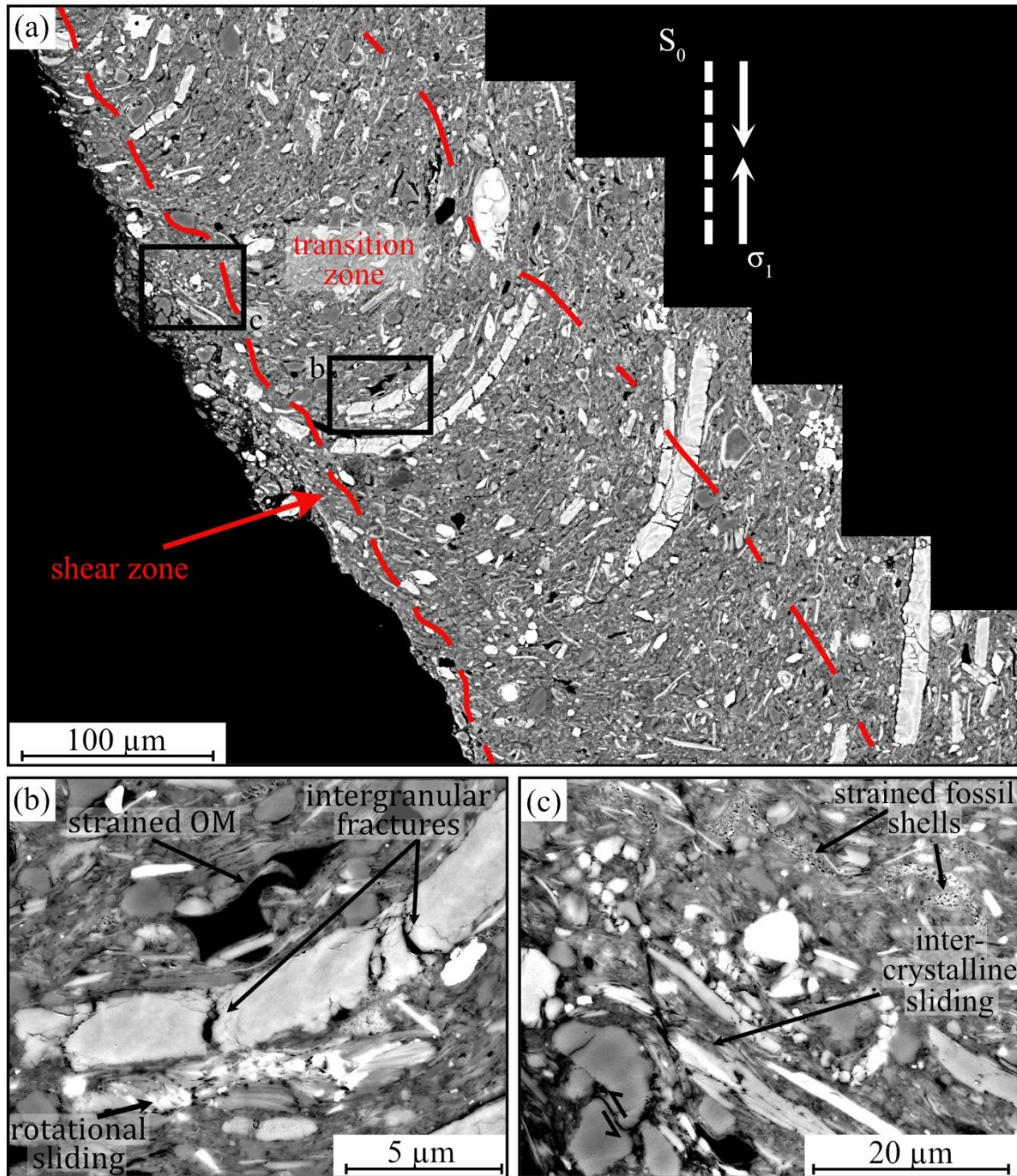


530

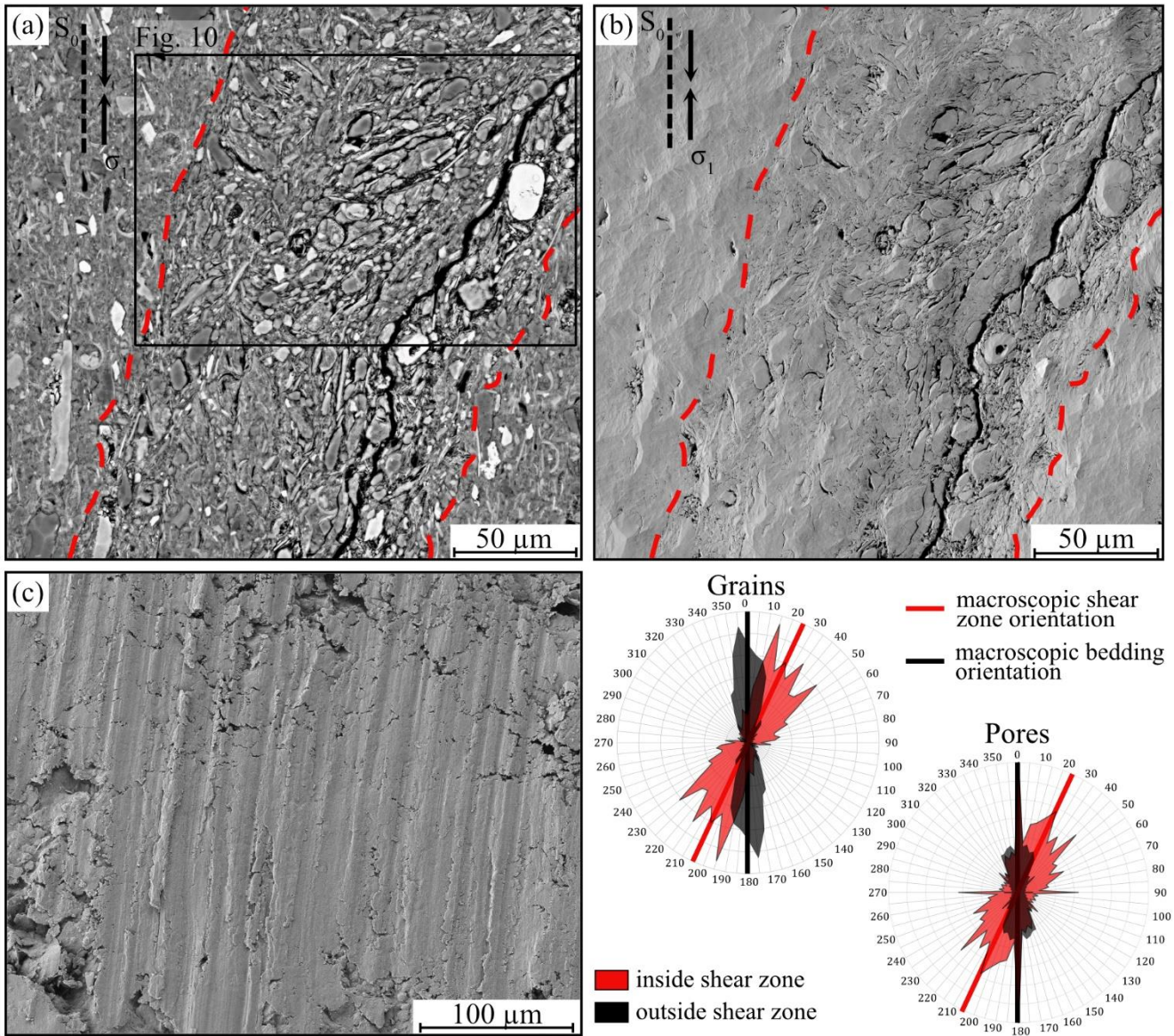
Figure 6: Macroscopic structures of deformed samples show shear bands, whose inclinations decrease with respect to horizontal with higher effective confinements. BSE-images show the mesoscopic view of the shear band, consisting of multiple shear fractures (a) and b)), and elongated calcite grains present the relative shear displacement. We note here that based on our structural interpretation, the bedding orientation of one sample ($\sigma_c = 2.5$ MPa) is inclined by 84° instead of 90° from horizontal. However, we consider this small discrepancy of 6° insignificant for the analysis.



535 **Figure 7: SEM-images presenting mesoscopic and microscopic deformation structures for the samples deformed at 2.5 MPa effective consolidation stress. (a) shows a network of multiple, anastomosing fractures constituting one of the main shear fractures observed on the macro scale (a') shows kinking of minerals and disrupted, randomised microfabric in a shear zone. (b) displays a dilatant kink-band, which is characterised by a sharply kinked ca-bearing vein observed in the EDS-image (d).**



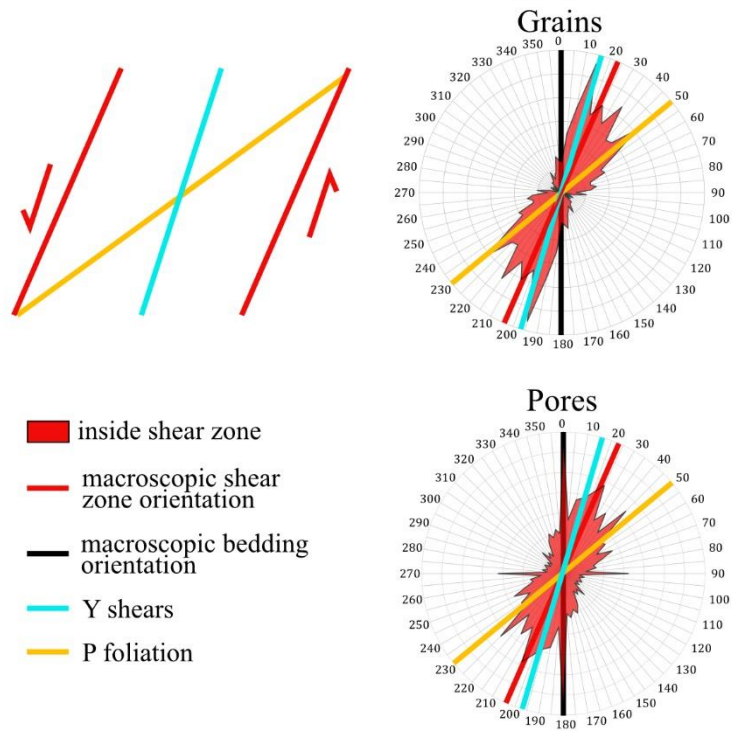
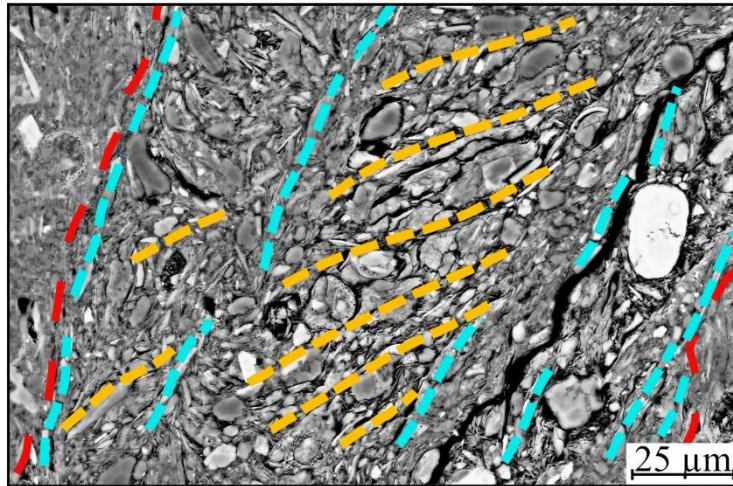
540 **Figure 8: SEM-BSE images presenting deformation structures of the samples tested at 16 MPa effective confinement. (a) shows the rotating fabric in the transition zone, which aligns to the shear zone. (b) presents typical grain-scale deformation markers such as intracrystalline rotational sliding, and stretching of fossil shells. Larger, elongated calcite grains hosts intragranular flexural fractures. (c) displays inter and intracrystalline sliding of phyllosilicates, and strained fossil shells leaving crushed trails aligned parallel to the shear zone direction.**



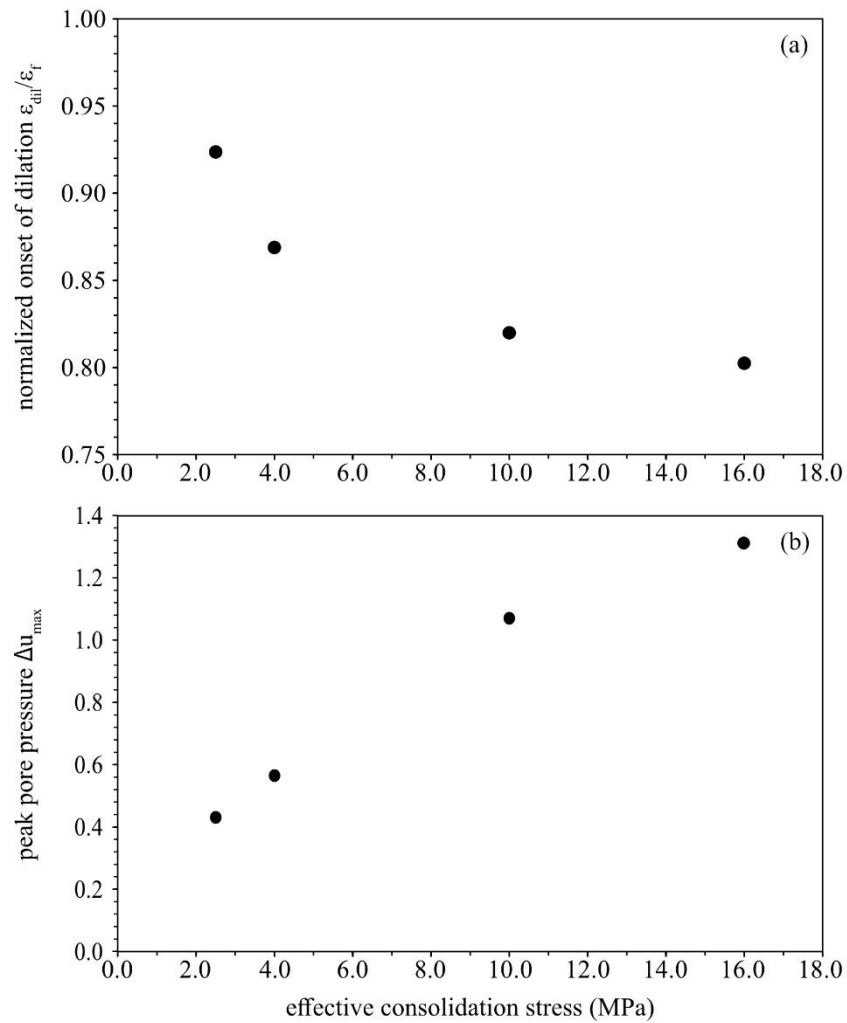
545

Figure 9: SEM-images of the sample deformed at 4 MPa effective confinement presenting the shear zone as well as orientations of grains, pores, and macroscopic structures. a) shows grain orientation (BSE-image) b) shows the increased apparent porosity in the shear zone, and c) displays the surface morphology of a shear plane (both SE2-images). Rose diagrams of grains and pore within and outside of the shear zones indicate the self-similarity of structure orientations across different scale magnitudes.

550



555 **Figure 10: Structures mapped in the shear zone (zoom-in from figure 9). Grain and pore orientation indicate the development of Y-shears and P foliation, which are both represented by orientation peaks of grains.**



560 | **Figure 1149:** (a) Axial strain at the onset of (net) dilation normalised by the respective axial strain at failure indicates an earlier (net) dilation at higher effective stresses. (b) Maximum change in pore water pressure during undrained loading increases with higher effective stresses. Both graphs show a strong non-linearity.

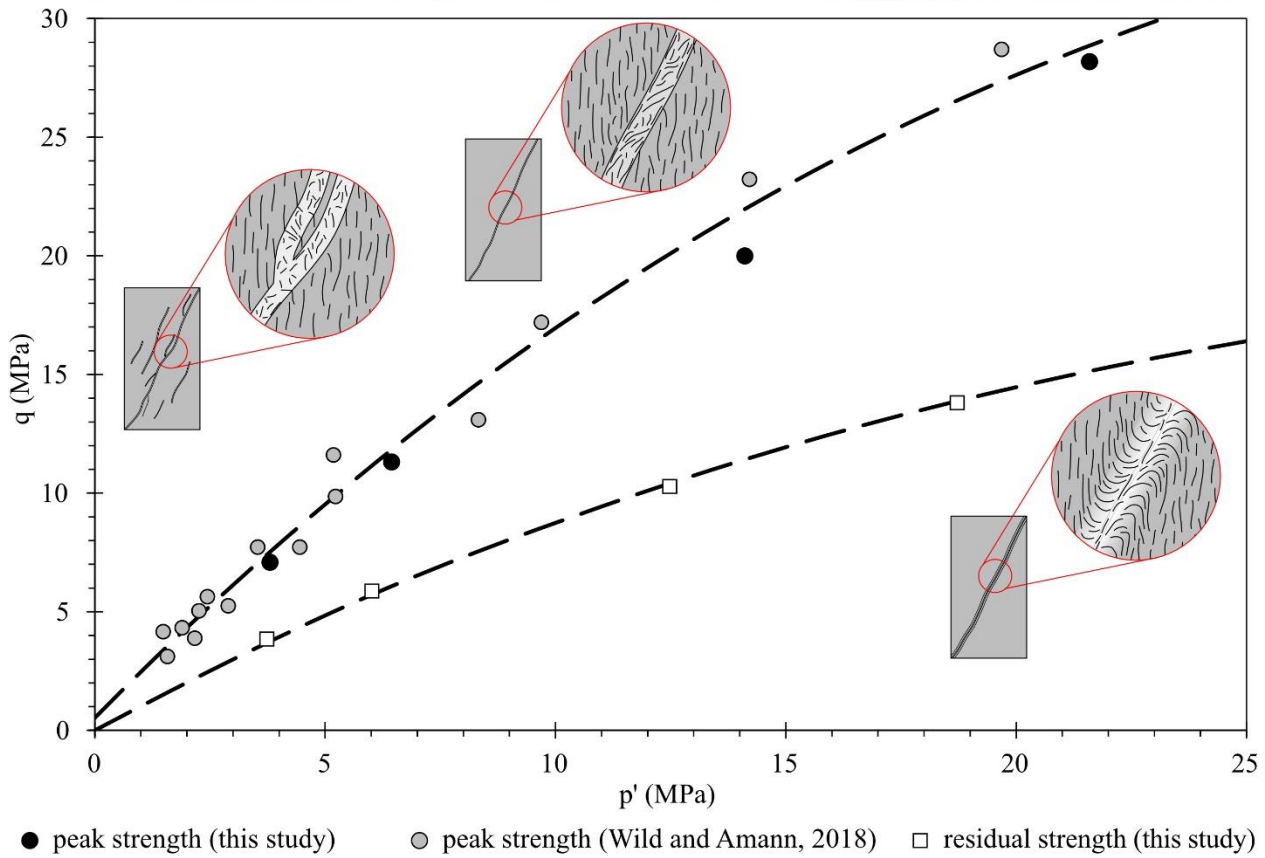


Figure 1244: Peak and residual effective strength of shaly Opalinus Clay under triaxial undrained compression and our microstructural model for shear failure. The non-linear failure envelopes, fitted through all data points, underlines the gradual transition for deformation microstructures from brittle to ductile and the tendency for suppression of dilatancy due to the reduction in shear zone porosity.

570

575

Table 1: Water content of samples before and after the experiment indication the resaturation of the samples.

Sample #	water content before testing (%)	water content after testing (%)
OPA-P-2.5	6.88	8.85
OPA-P-4	6.79	7.75
OPA-P-10	6.74	7.35
OPA-P-16	6.75	8.10

580

Table 2: Overview of experimental parameters (σ_c : total confining stress, u_0 : initial pore water pressure before shearing, σ'_c : effective confining stress before shearing) and elastic (E: Young's modulus, ν_L : Poisson's ratio), hydro-mechanical and strength parameters (q_f : differential stress at failure, q_r : residual differential stress, Δu_{max} : maximum change in pore pressure during shearing phase,).

Sample #	σ_c (MPa)	u_0 (MPa)	σ'_c (MPa)	E (GPa)	ν_L (-)	q_f (MPa)	q_r (MPa)	Δu_{max} (MPa)
OPA-P-2.5	5	2.5	2.5	4.01	0.74	7.1	3.86	1.08
OPA-P-4	6.5	2.5	4	5.92	0.63	11.32	5.88	1.41
OPA-P-10	12.5	2.5	10	7.04	0.62	20.01	10.28	2.67
OPA-P-16	19	3	16	7.75	0.62	28.20	13.81	3.93

585

Table 3: Parameters used for fitting the failure surface constrained by Eq. 1 to our data and those of Wild and Amann (2018a).

	μ	C	β
peak strength	2.0	0.5	0.0191
residual strength	1.0584	0	0.0191